vehicles

MDPI

Article

EV Battery Degradation Assessment Under Standard Drive Cycles Using Simulated EIS

Akila E. Jayasinghe [1,2,3], Nuwantha Fernando [1,*], Sisil Kumarawadu [2], Liuping Wang [1] and J. P. Karunadasa [2]

[1] Department of Electrical and Electronic Engineering, School of Engineering, RMIT University, Melbourne VIC 3000, Australia; s3941392@student.rmit.edu.au (A.E.J.); liuping.wang@rmit.edu.au (L.W.)
[2] Department of Electrical Engineering, Faculty of Engineering, University of Moratuwa, Moratuwa 10400, Sri Lanka; sisil@uom.lk (S.K.); karunadasaj@uom.lk (J.P.K.)
[3] Department of Engineering Technology, Faculty of Technology, University of Jaffna, Jaffna 40000, Sri Lanka
* Correspondence: nuwantha.fernando@rmit.edu.au

Abstract: Lithium-ion batteries (LIBs) play a critical role in electric vehicles (EVs) and hybrid electric vehicles (HEVs) and degradation of LIBs influences lifetime, reliability, safety and dependability. The ability to assess and quantify degradation enables assessment of LIB's true state of health. This paper investigates LIB degradation using a pseudo two-dimensional (P2D) model, particularly focusing on the changes to Electrochemical Impedance spectroscopy (EIS) results due to degradation. Three key degradation mechanism are considered and the impact of State-of-Charge (SoC) and temperature on EIS results are discussed. This paper also identifies the need for a more realistic approach to assess degradation. Simulations are conducted considering four repetitive standard drive cycles (viz., HTDDT, HWFET, US06 and OCTBC) for a vehicle travel distance of 150,000 km for each case. The cycle counting method is used to convert partial SoC variations during a drive cycle to an equivalent full cycle count which is then used within the degradation model to modify the parameters to represent the P2D model. This study demonstrates a robust process for analyzing degradation dynamics. The methodology presented here can guide future researchers with experimental data, enabling validation and refinement of model parameters to advance LIB degradation analysis and improve battery life predictions under operational scenarios.

Keywords: electric vehicles; hybrid electric vehicles; lithium-ion battery degradation; battery modelling; impedance spectroscopy

check for updates

Academic Editor: Yiqun Liu

Received: 6 December 2024
Revised: 16 February 2025
Accepted: 17 February 2025
Published: 19 February 2025

Citation: Jayasinghe, A.E.; Fernando, N.; Kumarawadu, S.; Wang, L.; Karunadasa, J.P. EV Battery Degradation Assessment Under Standard Drive Cycles Using Simulated EIS. *Vehicles* **2025**, *7*, 21. https://doi.org/10.3390/vehicles7010021

Copyright: © 2025 by the authors. Licensee MDPI, Basel, Switzerland. This article is an open access article distributed under the terms and conditions of the Creative Commons Attribution (CC BY) license (https://creativecommons.org/licenses/by/4.0/).

1. Introduction

A long battery life is essential for EVs and HEVs due to economical viability since the battery may cost up to 30% of the total price of the vehicle [1]. Research has shown the importance of ageing and degradation modelling in determining battery performance in addition early detection of of battery failures in EVs and HEVs. Calendar ageing and cycle ageing are the two methods that affect battery degradation. However, the degradation linked to cycle ageing remains to be further investigated and eventually leads to issues such as internal short circuits, overcharging, over-discharging, and capacity fading [2,3]. The degradation of batteries in EVs or HEVs are also impacted by the regular charge and discharge events during driving and ambient conditions. Driving speed and acceleration are related to charge and discharge currents whereas the daily average use is related to the Depth of Discharge (DoD) [4].

Laboratory-based accelerated aging tests have been conducted in the past to analyze battery degradation in EVs. For example authors of [5,6] have studied the effect of cycling conditions, and the authors of [7] present how the different ageing mechanisms are related. While these laboratory tests mostly performed under controlled conditions at a specific loading cycle, a more useful assessment of ageing involves replicating real-life daily usage profiles, however is limited by the extensive time requirement. For example, it is reported that 10% reduction from the initial capacity of LIB cells may take up to 10 to 11 months even under accelerated conditions [4,8].

To predict degradation of batteries and assess lifetime under wide ranging operating conditions, model-based approaches have been proposed and can provide significant amount of the information [9,10]. These methods use physics-based [9,11], empirical [12,13], or data-driven [14,15] models to simulate degradation mechanisms which significantly reduces the reliance on time-intensive experimental testing. In model-based approaches, it is important to analyze the different degradation mechanisms and how these mechanisms are incorporated into battery models. Degradation is brought on by a variety of conditions such as high charge/discharge rates and extremely high temperatures which contribute to different degradation modes that can manifest as battery capacity fade or power fade in the battery [16–18]. The most common degradation modes are; Loss of Lithium Inventory (LLI), Loss of Active Material (LAM), and Stoichiometric drift and impedance change [9]. The formation and growth of the Solid Electrolyte Interphase (SEI), the mechanical decomposition of the electrode materials, the dissolution of the transition metals from the cathode, and the deposition of metallic lithium in the anode lead to the different modes of degradation [2,3]. The most often reported degradation mechanisms in Li-ion cells are depicted in Figure 1, which is adapted from [2].

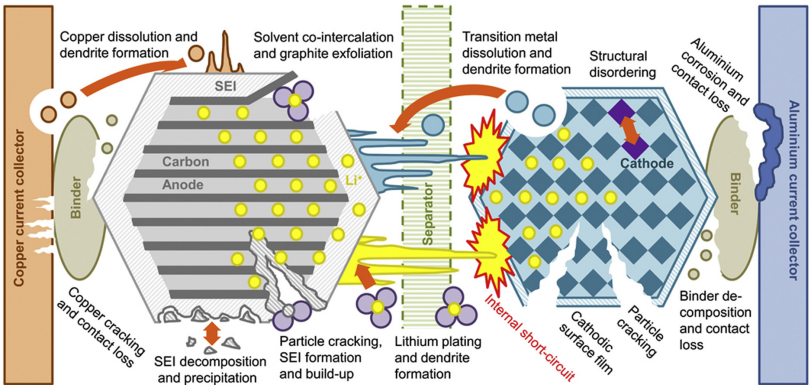


Figure 1. Degradation mechanisms in Li-ion cells [2].

The authors of [9] extend the Doyle–Fuller–Newman (DFN) model by including a strongly coupled degradation model in the graphite negative electrode and is implemented in PyBaMM [19]. Three degradations models are:

1. Solvent diffusion-limited SEI layer growth model
2. Li plating model
3. Particle cracking model

The following subsection describes these three degradation mechanisms in more detail.

1.1. Degradation Mechanisms

The three degradation models based on the following mechanisms proposed in [9] have been considered for the analysis.

1. SEI Layer Growth; the SEI is a passivation layer that forms spontaneously by electrochemical reduction of the carbonate-based organic electrolyte on the surface of

the negative electrode when its potential falls below the minimum thermodynamic stability potential of the electrolyte components. The kinetics of the reaction depend on a number of parameters, and SEI growth can continue during ageing and obviously reactivate on exposed negative electrode material surfaces (cracking, particle swelling during lithiation, variable porosity, delamination etc.) [2,7].

2. Li Plating; Li plating occurs when the potential of the negative electrode is <0 V vs. Li+/Li. At the end of charge and/or when the resistance R and current I are sufficiently high to induce a polarization U = RI greater than the difference between the LiC6 potential and that of Li+/Li. Low-temperature consequence is the increase of R (Arrhenius law) [2,7].
3. Particle Cracking; During cycling, the electrode's volume significantly changes; for example, when graphite lithiates, it expands, and when it de-lithiates, it contracts. Consequently, mechanical stress is created by concentration gradients within the particles, which may lead to the formation of cracks. Higher currents and larger particle sizes cause cracking to happen more severely. Toward the end of battery life, complete fracture can occur, often close to the separator, due to the higher local reaction current density during cycling [2,7].

EIS based analysis is typically used in characterizing the battery condition and can also indicate the level of degradation and the modes of degradation that has occurred in a battery. The following section reviews the different techniques developed in analyzing battery degradation using EIS based techniques.

1.2. Electrochemical Impedance Spectroscopy (EIS)

EIS has been used in the past as a fast, non-invasive, and reliable approach to access battery degradation and uses the application of a low-amplitude sinusoidal current or voltage over a range of frequencies to characterize the impedance [20]. A typical EIS spectrum of a LIB cell may consist of a semi-arcs in the mid-frequency range as shown in Figure 2. In a typical EIS, the high-frequency region reflects inductive behavior resulting from the reactance of metallic components, such as the connection cables and other conductive elements in the battery. The real impedance at the intersection with the x-axis represents the pure ohmic resistance, encompassing all resistive elements within the battery. The first semi-circle observed in the plot corresponds to the solid electrolyte interface (SEI) layer formed on the anode surface during cycling, which contributes to a gradual increase in internal resistance. The second semi-circle represents the charge transfer processes occurring at the electrode-electrolyte interface, while the low-frequency region illustrates the electron diffusion processes within the battery electrodes. In this context, when estimating internal resistance and State of Health (SoH) using EIS, the medium and low frequencies are typically considered [21].

EIS has also been used for battery degradation analysis based on impedance variation in different frequency bands [22–26]. In [11], EIS measurements were taken for 100% and 50% State of Charge (SoC) levels in the frequency range of 0.025 Hz to 4 kHz. It has been identified that the charge-transfer resistance and SEI film resistance have a clear trend with cycle ageing which demonstrates that it can be used for SoH estimation. Similarly, a mathematical model for simulating EIS was proposed in [22] which is based on a novel thermo-electrochemical model. The double-layer capacitance also has been considered in [22] and it has been identified that when the SEI layer growth reaches its equilibrium point the EIS response becomes stable which allows analysis of the impact of the degradation mechanism on the impedance response.

The authors of [23] used EIS as an offline analysis method for parameter identification of an Equivalent Circuit Model (ECM) with application to SoH and Remaining Useful Life

(RUL) estimation. The equivalent circuit used in this method contains five elements, out of which two are for model resistance namely ohmic resistance and SoC-dependant resistance, and two constant phase elements (CPEs) for diffusion, charge transfer, and chemical processes modeling and a voltage source. The EIS was observed from the measurement taken at 298 K and frequency range from 0.01 Hz to 10 kHz. Both the battery's equivalent series resistance (ESR) in ECM and remaining capacity have been predicted by this technique using simulated data. The average absolute error of the estimated remaining battery capacity is shown to be 2.1%, demonstrating the practicality and precision of the suggested techniques. The correlation between the SEI resistance which is considered as the resistance of the second CPE of ECM considered and the SoH has been revealed in [24] which has a prediction error less than 3%. It has limitations since the temperature has not been considered. Similarly, the authors of [25,26] estimate the SoH based on the ohmic resistance of ECM and results are validated for both standard and abnormal batteries, and the maximum error obtained for them are found to be 3.73% and 8.66%.

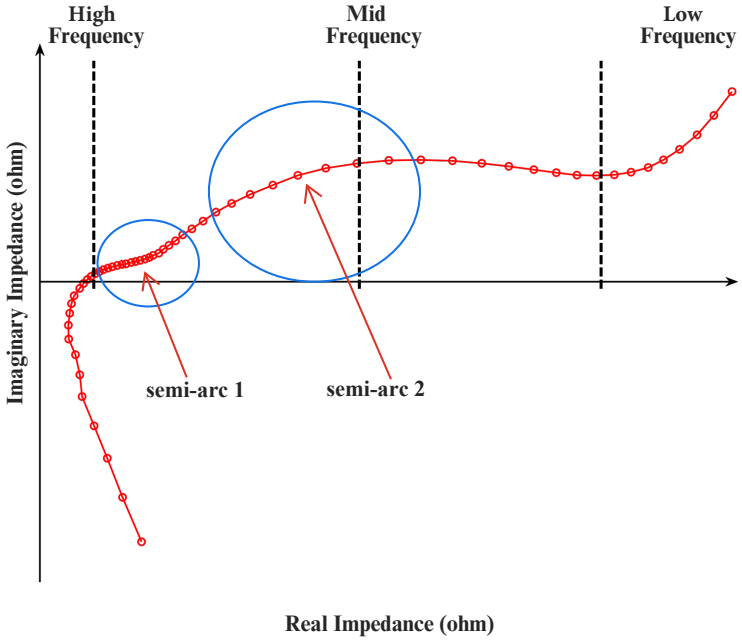


Figure 2. Representation of the frequency regions on a Nyquist plot.

Research has also progressed to include both temperature and SoC in EIS analysis since varying temperatures and SoC states impact the accuracy of SoH estimation [27]. As a result, an improved version of the SoH estimation method is proposed in [28] which considers the SoC, temperature, and charge-transfer resistance. The authors of [29] examine the calendar ageing phenomenon of LIB cells utilized in HEVs and suggest an RUL prediction method for it. The real impedance at 0.1 Hz is identified through EIS analysis by the authors of [29] and is selected as a reliable empirical indicator for forecasting the SoH due to its exponential correlation with So. The authors claim that this indicator offers a concise and actionable metric that simplifies EIS data while retaining diagnostic value. Similarly in [30], the EIS for LIB was obtained for different SoC levels and temperatures and the number of aging cycles. The charge transfer resistance is estimated using the EIS data which is used to determine the SoH of the LIB cell. In contrast, a simple-multi point impedance technique has been proposed in [31] which is less complicated than obtaining a complete EIS. It has been validated that this method has higher efficiency compared to the other methods.

In typical EIS characterization, the LIB cell is assumed to have a linear system response whereas in reality, it does not. By assuming that the battery cell has a linear system

response it is conventionally fitted to an ECM which contains basic electrical elements such as resistors, capacitors, and also some ad hoc components such as CPEs. Since the LIB contains nonlinearities, assuming a linear response will not correctly reflect the battery characteristics. The authors [20] present a non-linear EIS technique referred to as Non-Linear Electrochemical Spectroscopy (NLEIS) which uses a larger amplitude sinusoidal input current to capture the non-linearities of the LIB cell. This analysis is based on the assumption of a Single Particle Model (SPM) with unbalanced charge transfer kinetics at the surface of the electrode particles and nonlinear diffusion of lithium within them. Based on this model and the assumption of a reasonably small excitation amplitude, which is appropriate to produce accurate fits to impedance data, they systematically derive analytical equations for the impedance up to the second harmonic response.

According to the aspects discussed above, it is observed that EIS based techniques have been widely used in analyzing battery degradation. Section 3 of this paper investigates the impact of different battery conditions such as SoC and Temperature on the EIS results using simulations. Section 4 of this paper investigates the impact of battery cycling and particularly presents a technique to obtain a simulated EIS result under cyclic loading using standard drive cycles.

This paper aims to demonstrate the capability of utilizing the DFN model in conjunction with EIS analysis to extract and analyze the potential variations in EIS arising from different physical phenomena associated with degradation models. By integrating equivalent full cycle counting to account for partial state-of-charge fluctuations in drive cycles, the paper provides a comprehensive framework for evaluating the impacts of key degradation mechanisms including SEI layer growth, lithium plating, and particle cracking on battery performance, thereby advancing the understanding of LIB aging under dynamic operational scenarios. While the study does not include experimental results, the proposed methodology provides a foundation for future researchers to analyze battery degradation due to cycle ageing using electrochemical models integrated with degradation sub models, once experimental data becomes available.

It is also worth noting that by utilizing the PyBaMM tool, this work provides a clearer understanding of how various degradation processes affect EIS. Rather than relying on time-consuming experimental data, these simulations help to illustrate the evolution of physical parameters under different conditions, thus enhancing the understanding of degradation mechanisms in battery systems where future researchers can test different condition monitoring algorithms and degradation monitoring and assessment strategies rapidly.

The implementation of the simulation of the battery is presented in the following section.

2. Battery Simulation and Degradation Modelling

This paper uses the DFN model coupled with the degradation sub-models for the degradation analysis. The DFN model is described with six governing equations listed in [32] where a detailed description and definition of the DFN model can be found.

The DFN model's geometry is depicted in Figure 3. The domain $0 \leq r \leq R_k$ (for $k \in \{n, p\}$) defines the two averaged electrode particles where the subscripts n and p denote the negative and positive electrodes, respectively and r denotes the radial coordinate within a particle. The domain for the electrolyte is $0 \leq x \leq L$ and includes the negative electrode $0 \leq x \leq L_n$, the separator $L_n \leq x \leq L - L_p$, and the positive electrode $L - L_p \leq x \leq L$, where L_p and L_n are the thickness of positive and negative electrode respectively and x denotes the spatial coordinate along the thickness of the cell.

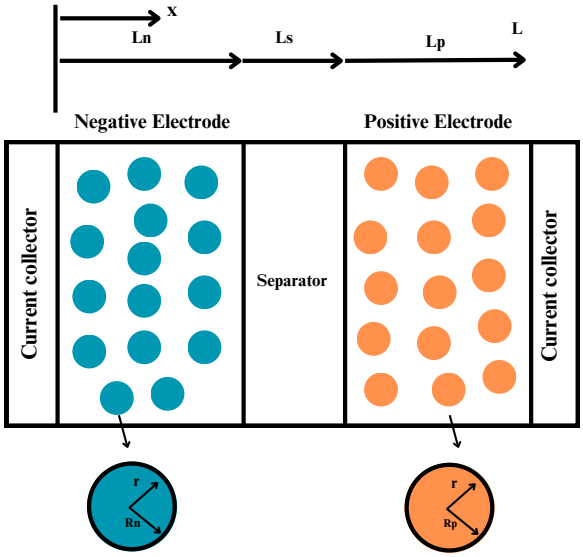


Figure 3. DFN Model Schematic Diagram [32].

2.1. SEI Layer Growth Model

The solvent diffusion limited SEI layer growth model proposed in [9]. It assumes that the diffusion of solvent molecules through the SEI layer limits its growth as introduced in [33].

The flux of the solvent molecules follows Fick's law assuming the steady state conditions. The flux of solvent molecules given by;

$$N_{sol} = -D_{sol}(T)\frac{\partial c_{sol}}{\partial l} \tag{1}$$

where c_{sol} is the solvent concentration with an initial value of 0 mol/m^3 at $l = 0$ m and $c_{sol,0}$ at $l = L_{SEI}$, $c_{sol,0}$ is the solvent concentration in the electrolyte, $D_{sol}(T)$ is the solvent diffusion coefficient, T is operating temperature, l is one location of the SEI layer and L_{SEI} is the thickness of the SEI layer and The solution becomes:

$$N_{sol} = -\frac{c_{sol,o}D_{Sol}(T)}{L_{SEI}} \tag{2}$$

According to the conservation of mass, the interfacial flux density of the SEI layer is:

$$N_{SEI} = -N_{sol} = \frac{c_{sol,o}D_{Sol}(T)}{L_{SEI}} \tag{3}$$

Therefore, the SEI layer thickness growth rate can be expressed as:

$$\frac{\partial L_{SEI}}{\partial t} = -\frac{1}{2}N_{sol}\bar{V}_{SEI} = \frac{c_{sol,o}D_{Sol}(T)\bar{V}_{SEI}}{2L_{SEI}} \tag{4}$$

where V_{SEI} is SEI partial molar volume. As per the equation for SEI layer thickness growth rate the key parameter is $D_{Sol}(T)$ has an Arrhenius temperature dependence that can be expressed as:

$$D_{\mathrm{Sol}}(T) = D_{\mathrm{Sol}}(T_{\mathrm{ref}})\exp\left(-\frac{E_{\mathrm{sol}}}{RT} + \frac{E_{\mathrm{sol}}}{RT_{\mathrm{ref}}}\right) \tag{5}$$

where E_{sol} is activation energy of diffusion process , R is universal gas constant and T_{ref} is the temperature where $D(T_{ref})$ is measured. And at last the Voltage drop (η_{SEI}) due to the SEI growth can be expressed as $\eta_{\mathrm{SEI}} = \rho_{\mathrm{SEI}} L_{\mathrm{SEI}} \frac{j_{\mathrm{tot}}}{a_-}$ where ρ_{SEI} is ohmic resistivity and j_{tot} is the interfacial current density.

2.2. Li Plating Model

The majority of Li plating models found in literature do not take into account the eventual breakdown of the plated Li into SEI and "dead lithium." The literature presents a variety of models resulting from the three-way interaction between plating, stripping, and SEI generation [34,35]. Since there are no strong couplings in any of these models, a new model in which plated Li gradually turns into dead Li is proposed in [9]. Accordingly, irrespective of the form of Butler Volmer Equation [32] used, the concentration of plated Li ($c_{Li}(x,t)$) can be obtained by solving the differential equation:

$$\frac{\partial c_{Li}}{\partial t} = -a_- N_{Li} - \gamma\, c_{Li} \tag{6}$$

Here the time-limited decay (γc_{Li}) has been added as a second term to consider the concentration of dead lithium (c_{dl}) to the model which has the relationship of $\frac{\partial c_{dl}}{\partial t} = \gamma c_{Li}$. The decay rate γ is not a constant since it has been assumed that a reaction with electrolyte solvent is required to turn the plated Li into dead Li. As a result, it is diffusion-limited similar to SEI formation reaction. This can be modeled by making it dependent on the SEI thickness L_{SEI}.

$$\gamma(L_{SEI}) = \gamma_0 \frac{L_{SEI,0}}{L_{SEI}} \tag{7}$$

where $L_{SEI,0}$ is the SEI thickness at t=0 and γ_0 is a fitting parameter. Now the Butler-Volmer equation can be updated with variable transfer coefficient ($\alpha_{a,Li}$) and ($\alpha_{c,Li}$).

$$N_{Li} = k_{Li}\left(c_{Li}\exp\left(\frac{F\alpha_{a,Li}\eta_{Li}}{RT}\right) - c_e \exp\left(-\frac{F\alpha_{c,Li}\eta_{Li}}{RT}\right)\right) \tag{8}$$

where $\eta_{Li} = \phi_s - \phi_e - \eta_{SEI}$.

2.3. Particle Cracking Model

During (de)lithiation, electrode materials undergo significant volume changes. The stress that follows can result in particle cracking, which produces new surfaces and accelerates side reactions like Li plating and SEI development [9]. In literature, a number of cracking models have been introduced. They can be categorized as empirical models and physical models [36]. The physical models have the advantage of performing accurately in high C-rates whereas empirical models will perform only for moderate C-rates.

In this paper, the particle cracking model based on [9] based on the fatigue crack model proposed in [36] is adopted as implemented in PyBaMM [19]. Particle cracking occurs due to the stress that the particles are experiencing. Therefore, at the particle level a stress model has been used in [36]. Accordingly, the radial stress σ_r, tangential stress σ_t and displacement u solutions are given by [9]:

$$\sigma_r = \frac{2\Omega E}{1-v}\left[c_{avg}(R_i) - c_{avg}(r)\right] \tag{9}$$

$$\sigma_t = \frac{\Omega E}{1-v}\left[2c_{avg}(R_i) + c_{avg}(r) - \bar{c}/3\right] \tag{10}$$

$$u = \frac{(1+v)}{(1-v)}\Omega r c_{avg}(r) + \frac{2(1-2v)}{(1-v)}\Omega r c_{avg}(R_i) \tag{11}$$

where E is the Young's modulus, Ω is the partial molar volume, v is Poisson's ratio, R_i is the radium of particle and $c_{avg}(r)$ is for average Li+ concentration between 0 and r given by [9]:

$$c_{avg}(r) = \frac{1}{3r^3}\int_0^1 \bar{c}r^2 dr \tag{12}$$

It is important to note here that $\bar{c} = c - c_{ref}$ represents the departure in lithium concentration from the c_{ref} which is the reference value for a stress-free scenario. From 9 to 11 it can be identified that the magnitude of stress is determined by particle radius and lithium concentration.

During the charge and discharge cycles the particles of the electrode experience cyclic stress load which leads to fatigue cracking. It is assumed that identical micro-cracks on the electrode particle surface with a length l_{cr}, a width w_{cr}, and a crack density of number per unit area ρ_{cr} and crack grow in length during cycling given by Paris' law, with the width and density remain constant.

$$\frac{dl_{cr}}{dN} = \frac{k_{cr}}{t_o}\left(\sigma_t b_{cr}\sqrt{\pi l_{cr}}\right)^{m_{cr}} \qquad \sigma_r > 0 \tag{13}$$

where t_o is the time for one cycle, b_{cr} is the stress intensity factor correction, k_{cr} and m_{cr} are constants based on experimental data. It is assumed that the tensile strength contributes only to crack growth which is denoted by $\sigma_r > 0$.

2.4. Lumped Thermal Model

PybaMM [19] has an inbuilt lumped thermal model based on [37]. This lumped thermal model is defined by the average temperature given by the following ordinary differential equation.

$$\rho_{eff}\frac{\partial T}{\partial t} = \bar{Q} - \frac{hA}{V}(T - T_\infty) \tag{14}$$

where ρ_{eff} is the effective volumetric heat capacity, T is the temperature, t is time, $\bar{Q}$ is the averaged heat source term, h is the heat transfer coefficient, A is the surface area (available for cooling), V is the cell volume, and T_∞ is the ambient temperature. It is necessary to specify an initial temperature, T_0. The effective volumetric heat capacity is computed as:

$$\rho_{eff} = \frac{\sum_k \rho_k c_{p,k} L_k}{\sum_k L_k} \tag{15}$$

where ρ_k is the density, $c_{p,k}$ is the specific heat, and L_k is the thickness of each component. The negative current collector, negative electrode, separator, positive electrode, and positive current collector of each corresponding component are denoted by the subscript $k \in \{cn, n, s, p, cp\}$. The heat source term ($Q = Q_{ohm,k} + Q_{rxn,k} + Q_{rev,k}$) accounts for Ohmic heating ($Q_{\text{ohm},k}$) due to resistance in the solid and electrolyte, irreversible heating ($Q_{\text{rxn},k}$) due to electrochemical reactions such as lithium intercalation/deintercalation at the electrodes, side reactions like SEI formation and electrolyte decomposition, and reversible heating ($Q_{\text{rev},k}$) due to entropic changes in the electrode. These terms can be calculated from $Q_{ohm,k} = -i_k \nabla \phi_k$, $Q_{rxn,k} = a_k j_k \eta_k$, $Q_{rev,k} = a_k j_k T_k \frac{\partial U}{\partial T}\Big|_{T=T_\infty}$ where i_k is the current, ϕ_k is the potential, a_k is the surface area to volume ratio, j_k is the interfacial current density, η_k is the over-potential, and U is the open-circuit potential. The averaged heat source term is computed by taking the volume average of Q.

The SEI layer growth, lithium plating, and particle cracking models, along with their interactions, have been rigorously validated by the authors of [38] against experimental data, including voltage, capacity, and resistance. Additionally, the coupled degradation sub-models

were tested under varying temperatures and validated for three key degradation modes: Lithium Loss Inventory (LLI) and Loss of Active Material (LAM) in both electrodes, as reported in [38]. At this stage of the research, the authors have chosen to adopt the existing models in their current form, as they have been previously validated by other researchers [38–40]. This approach was necessitated by the lack of comprehensive Electrochemical Impedance Spectroscopy (EIS) data suitable for the scope of this analysis. Future research has the potential to build upon this work by incorporating experimental data to validate the presented results, thereby strengthening the methodology and expanding its practical applicability.

The following section presents the impact of battery states on the EIS results using simulations on a cylindrical LG M50 21700 (LGM50) cell and also discusses the impact of battery degradation on these states.

3. Impact of Battery States on EIS Results

This section discusses the EIS simulation process using PyBaMM and explores key observations from the simulations, emphasizing the role of SoC and temperature on impedance behavior. The strategy outlined in Figure 4 is adopted to obtain simulated EIS for different LIB conditions. The simulated EIS strategy begins by setting initial conditions for the battery model. Subsequently, EIS parameters, including the frequency range (0.1 mHz to 100 Hz) and current amplitude (1 mA), are defined. A sinusoidal current function is generated as a function of time, with frequency as an input parameter. The PyBaMM simulation object is then created using the aged battery model, specified parameters, and a Casadi solver.

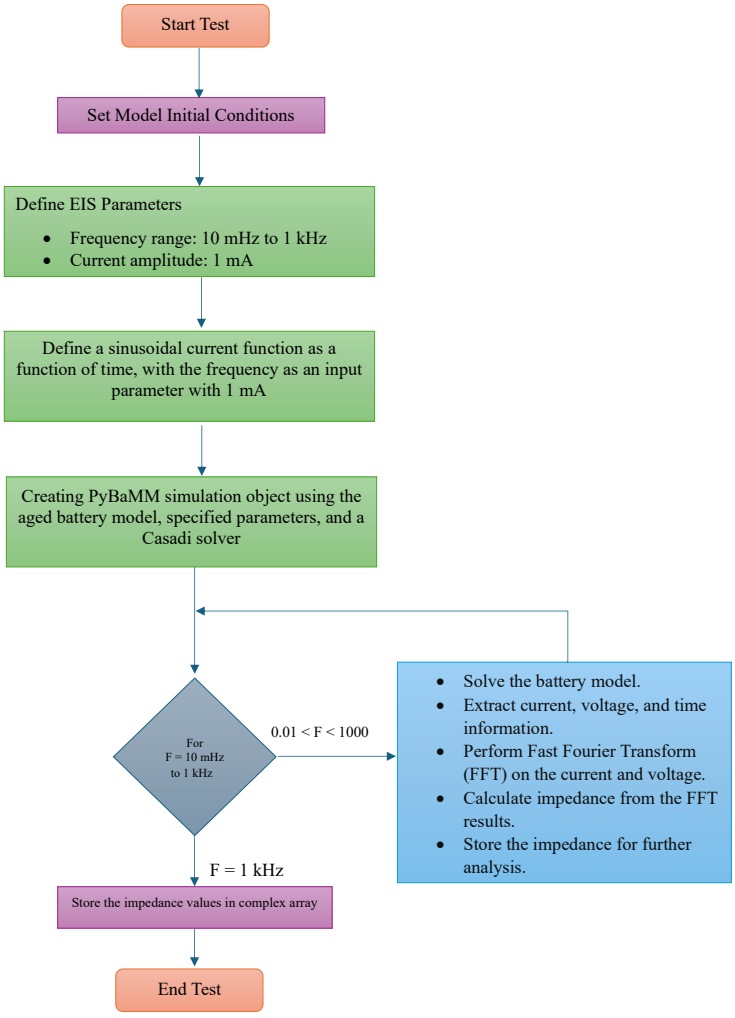


Figure 4. EIS Algorithm in PyBaMM.

The battery model is subsequently solved to extract current, voltage, and time information. A Fast Fourier Transform (FFT) is performed on the current and voltage and the impedance is calculated from the FFT results and stored for further analysis. This process is repeated for different frequencies within the defined range. Finally, the impedance values are stored in a complex array, and the simulation ends. The data set available in PyBaMM from [41] for LGM50 cell was chosen for the simulation. The specifications of LGM50 cell are listed in Table 1.

Table 1. Battery Cell Specifications [42].

Parameter	Details
Nominal Capacity	5000 mAh (5.0 Ah)
Nominal Voltage	3.6 V
Maximum Voltage	4.2 V (fully charged)
Minimum Voltage (Cut-off)	2.5 V
Energy	18 Wh
Standard Charge Current	Typically 0.5 C (2.5 A)
Maximum Continuous Discharge Current	1.5 C
Internal Resistance	Approximately < 25 mΩ at 1 kHZ
Chemistry	Nickel Manganese Cobalt Oxide (NMC 811/G+SiOx)

Analysis of Key Observations

Initially, EIS results were obtained for different SoC levels and an ambient temperature of 298 K using the PyBaMM DFN model. The battery model simulation was conducted with parameters published in [41,43]. The results shown in Figure 5 closely follow the trends observed in literature [28,30] and are significantly influenced by the SoC levels.

It is important to note that the parameter set used in this study is not intended to represent the true physical values of the system. Instead, these parameters were selected to achieve the best fit of the SEI models to experimental data reported in [41]. As such, they should be interpreted as effective parameters that enable the model to capture observed degradation trends rather than absolute physical constants. Also, the parameter set [41] considers the contact resistance (CR) as zero by default. However, alternative published data may inherently account for CR, which can lead to variations in impedance values of R_{ohm} which is the intersection point of EIS and the real impedance axis. As illustrated in Figure 5 this effect by comparing impedance spectra with CR of 0.015 Ω for SoC 0.9 indicated in brown. The inclusion of CR shifts the real-axis intercept and alters the overall impedance response, demonstrating its influence on the electrochemical behavior of the system, when the CR matched accordingly the EIS response is similar to the EIS responses reported in [44,45]. For the analysis of this paper, the default value for CR = 0 is considered.

The charge transfer resistance, often represented by the the diameter of the mid-frequency semicircle, is defined as the derivation of the voltage contribution from the spatially averaged overpotential, $\eta_{\pm}$, with respect to the current, evaluated at the operating point x_m (where $i = 0$). According to the derivation provided in [44], it can be approximated as:

$$R_{ct,m,\pm} \approx \frac{R_{ct,\pm}^{\text{typ}}}{2c_{m,\pm}(1 - c_{m,\pm})} \frac{1}{\sqrt{c_e x_m}}. \tag{16}$$

At high and low stoichiometric values $c_{m,\pm}$ (which correspond to high and low SOC), the charge transfer resistance increases, while at mid-range SOC values, the resistance decreases. This trend is consistent with the observed results. The variation of R_{ct} against SoC is shown in Figure 6 and these variations align closely with those reported in [44].

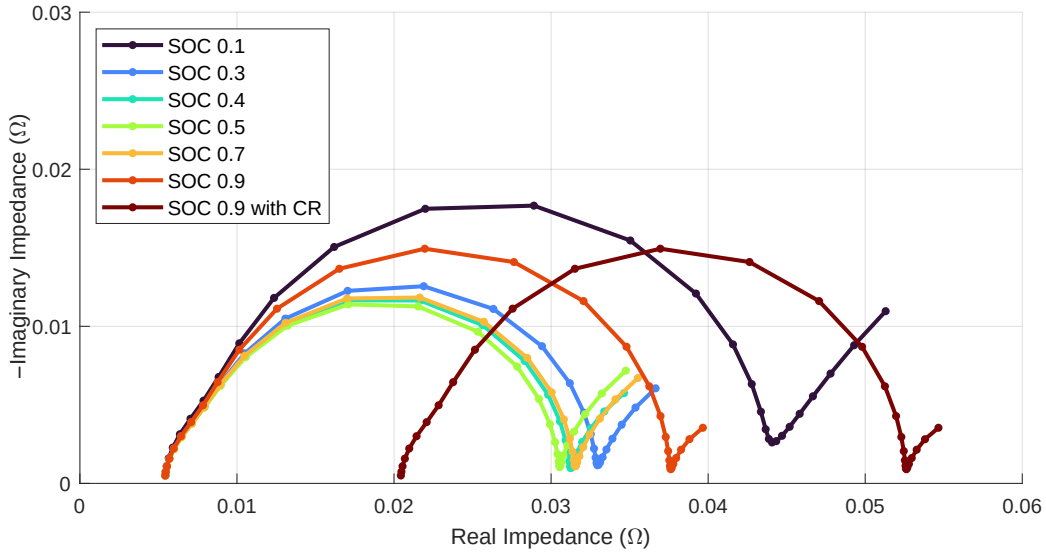


Figure 5. Simulated EIS for different SoC levels at 298 K.

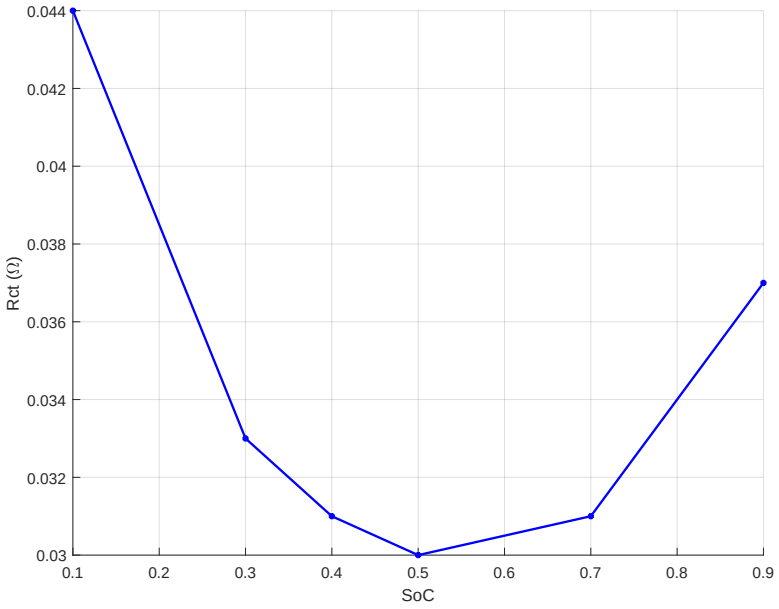


Figure 6. Variation of R_{ct} different SoC levels at 298 K.

Figure 7 illustrates the temperature-dependent behavior of the Nyquist plot, where the diameter of the semi-arc decreases with increasing temperature. Starting at room temperature (298 K), the diameter of the semi-arc which represents R_{ct} reduces approximately by 47% when the temperature is increased from 298 K to 318 K. Additionally, the central peak of the semi-arc displays pronounced variations in both real and imaginary components of the impedance. Specifically, for a 20 K temperature rise, both real and imaginary impedance decreases approximately 60%. These observations emphasize the significant influence of temperature on the electrochemical impedance properties of the system. It is well known that the internal electrochemical reaction rate in batteries is influenced by temperature and can be modeled using the Arrhenius law [46], outlined in (5) and the observation from this simulation exhibits the same behavior.

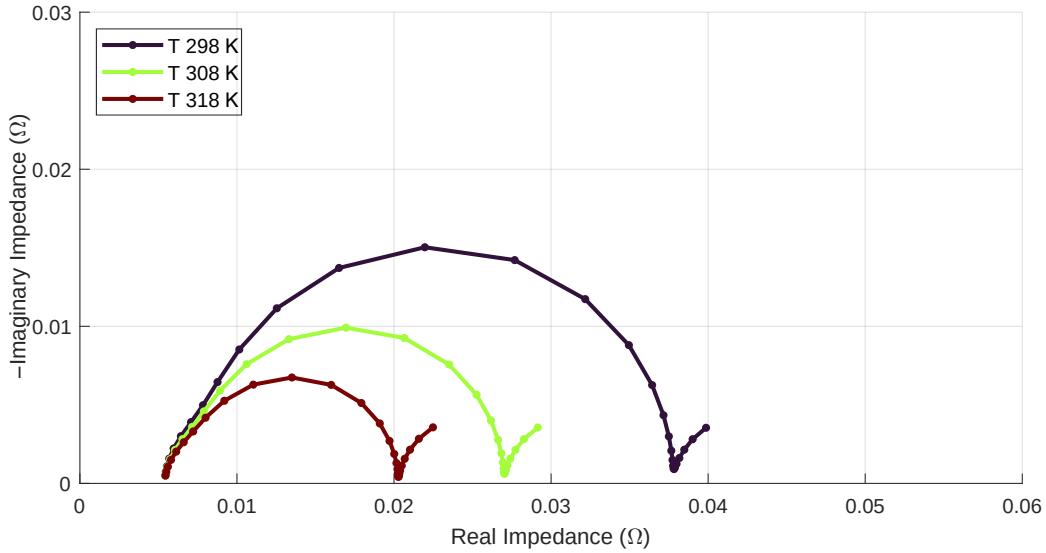


Figure 7. Simulated EIS for different initial temperature levels at SoC 0.9.

A summary of how each degradation mechanism interacts with different operational factors is presented in Table 2. SEI layer growth shows dependence on SoC because higher electrode potentials drive electrolyte decomposition reactions, while elevated temperatures accelerate the kinetics of these side reactions, and charge/discharge currents influence lithium-ion transport, intensifying SEI formation. Lithium plating, modeled in PyBaMM through over-potential-driven mechanisms, is observed at high SoC (where the anode potential approaches lithium deposition levels), low temperatures (which slow lithium diffusion), and high charge currents (which increase over-potential and plating likelihood). Particle cracking emerges in the simulation as a result of mechanical stress caused by repeated lithiation/delithiation, correlating with the number of cycles, and is exacerbated at high currents, which intensify stress on electrode particles. In the particle cracking model, the Paris' Law crack growth, cycle number is converted into time using the chain rule.

Table 2. Factors Affecting Degradation Mechanisms.

Degradation Mechanism	State of Charge (SoC)	Temperature (T)	Cycle Number	Charge/Discharge Current
SEI Layer Growth	✓	✓		✓
Lithium Plating	✓	✓		✓
Particle Cracking		✓	✓	✓

While the battery simulations presented in this section consider the impact of SoC, temperature and calendar ageing, a true assessment under realistic drive conditions need to include the impact of battery cycling. While the existing model considers a fixed cycle, a typical drive cycle may contain multiple partial cycles with varying degree of charge/discharge rates. The following section investigates an approach that incorporates these types of realistic conditions in the the simulation by an equivalent cycle counting approach.

4. Incorporating Drive Cycle Conditions in Battery Simulation

The degradation of batteries in EVs and HEVs is significantly influenced by driving patterns. Repeated charge and discharge events subject the batteries to stress, accelerating their cycle aging. Consequently, integrating drive cycle conditions into battery simulations is crucial for understanding the degradation behavior. In this section the drive cycle studies are conducted with the experimental drive cycle data available in [47]. This data is initially

used to calculate the equivalent standard number of cycles and then fed into the PyBaMM model simulation to analyze the degradation behavior. The equivalent full cycle count is derived by computing the DoD for each cycle and scaling partial cycles to their full-cycle equivalents, this method provides a measure of cumulative cycling stress experienced by the battery. The overall process for battery degradation with EIS for drive cycle conditions is outlined in Figure 8.

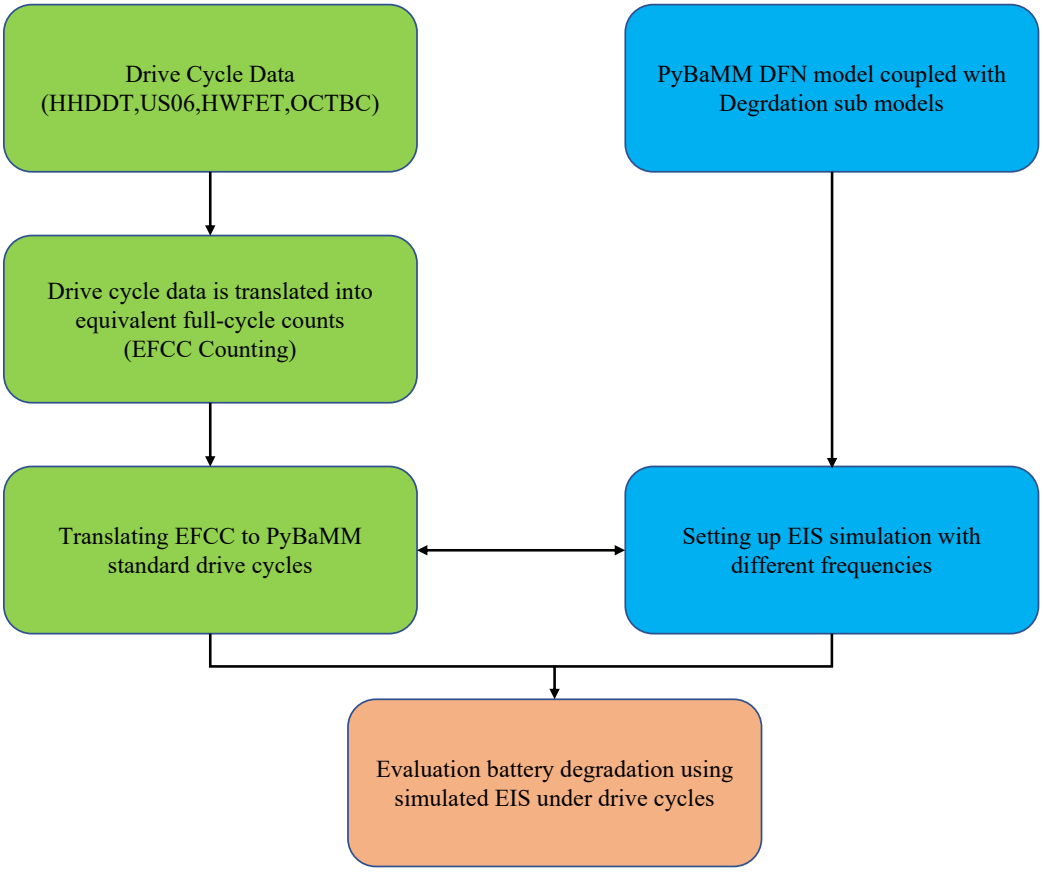


Figure 8. Overall process for incorporating drive cycle conditions.

4.1. Drive Cycle Dataset

The dataset published in [47] contains lithium-ion battery cycling data with 12 distinct drive cycles conducted under five ambient temperatures using three brand-new lithium-ion battery cells with a nominal capacity of 4.93 Ah. SoC values are calculated using Coulomb counting and the test has been using a BaSyTec CTS cycler in a Memmert climate chamber. A summary of drive cycle dataset is listed in Table 3.

Table 3. Summary of Drive Cycle Dataset.

Parameter	Details
Battery Cells	LG M50 21,700 Cells
Drive Cycles	12 cycles (4 repetitions per cell)
Drive Cycle Names	BCDC, LA92, HHDDT, CSHVC, FTP-72, FTP-75, HWFET, IM, US06, PDTCB, PDMHC, OCTBC
Ambient Temperatures	45 °C, 35 °C, 25 °C, 15 °C, 5 °C
Equipment Used	BaSyTec CTS cycler, Memmert climate chamber

4.2. Equivalent Cycle Count Calculation

In a practical drive cycle, the batteries may not always fully discharge/charge. As shown in Figure 9, the drive cycles show rapid and frequent current fluctuations with high C-rates which lead to numerous partial charge-discharge events. In order to quantify the battery cycle usage and its impact on degradation, battery cycle models have been proposed to accurately observe the impact of partial charge-discharge events.

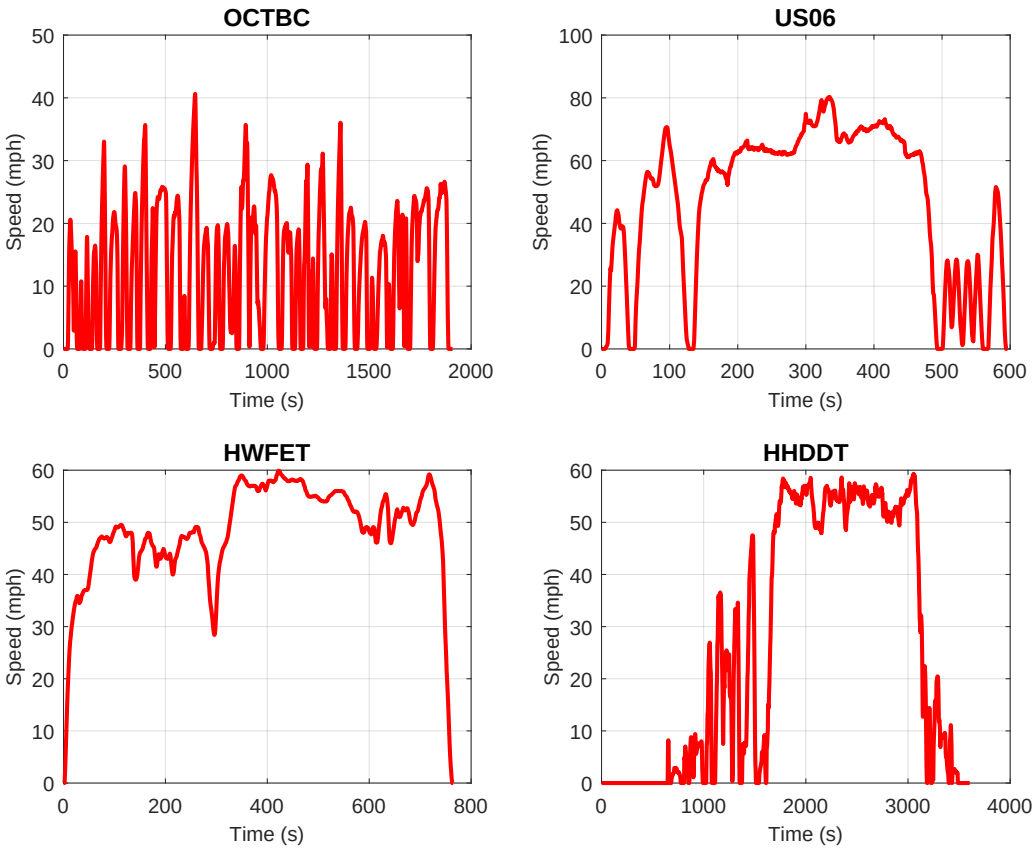


Figure 9. Standard speed profiles of example four drive cycles [48].

A cycle life model based on physical equations from fatigue theory and equivalent cycle, counting is proposed in [13]. In this work, the equivalent cycle counting method proposed in [13] was implemented in MATLAB 2023b and the equivalent number of cycles for different drive cycle conditions provided in [47] have been calculated. In this cycle counting approach, a cycle transition is detected by monitoring the sign change of the SoC derivative (ΔSoC). For each detected cycle, the DoD is computed as;

$$\mathrm{DoD} = 1 - \mathrm{SoC(n)} \tag{17}$$

An equivalent full cycle count (EFCC) is calculated to quantify the contribution of partial cycles to full battery charge/discharge cycles. The equivalent number of cycles for a specific DoD is defined as the number of full charge-discharge cycles equivalent to a scenario where the battery operates between 0% and 100% SoC. For instance, refer to Figure 10, if the battery discharges from 80% SoC (corresponding to 20% DoD) to 40% SoC (60% DoD) and then recharges to 60% SoC (40% DoD), the DoD for the cycle is 60% which is indicated in green line in Figure 10. The equivalent number of full cycles can then be calculated using:

$$EFCC = 0.5\left(1 - \frac{20}{60}\right) + 0.5\left(1 - \frac{40}{60}\right) \tag{18}$$

According to (18) the EFCC for any partial cycle can be calculated as follows [13]:

$$EFCC = 0.5\left(2 - \frac{\mathrm{DoD}_{n-2} + \mathrm{DoD}_{n}}{\mathrm{DoD}_{n-1}}\right) \quad (19)$$

The sum of EFCC across all partial cycles provides the total equivalent cycle count, representing the cumulative cycling effect experienced by the battery during the test. This algorithm is applied to drive cycle data for the 298 K ambient temperature condition and the EFCC has obtained. The following 4 drive cycles were selected for the comparison in this paper.

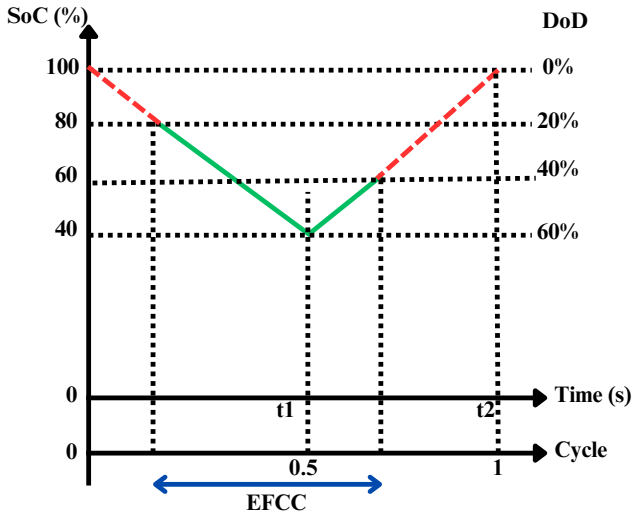


Figure 10. EFCC Concept [13].

1. Heavy Heavy-Duty Diesel Truck Composite Cycle (HHDDT): Evaluates fuel consumption and emissions for heavy-duty diesel trucks.
2. Highway Fuel Economy Test (HWFET): Measures highway fuel economy for light-duty vehicles.
3. US06 Supplemental Federal Test Procedure (US06): Tests aggressive driving behaviors.
4. Orange County Transit Bus Cycle (OCTBC): Simulates transit bus operations in urban and suburban environments.

The standard metrics [48] of the selected four standard drive cycles are listed in Table 4 below. The speed variation of standard drive cycle data is shown in Figure 9.

Table 4. Matrics of selected drive cycles [48].

Drive Cycle	Time (min)	Distance (miles)	Maximum Speed (mph)	Average Speed (mph)
HHDDT	60.08	26.05	59.3	26.01
HWFET	12.75	10.26	59.9	48.2
US06	9.93	8.01	80.3	48.3
OCTBC	31.83	6.54	40.63	12.33

The current profile of the experimental drive cycle data is shown in Figure 11 and the SoC variation with the time obtained using the Coulomb counting is shown in Figure 12. In the HHDDT cycle, as a result of high loads, high average currents are observed. Accordingly in the highways segment the SoC declines gradually whereas in urban segments the decline of SoC is sharper. In contrast, the HWFET cycle exhibits a low to moderate current which indicates steady highway driving. In US06 frequent dips in SoC can be seen as a

result of strong current peaks during fast acceleration and partial recovery during braking. The OCTBC has highly dynamic currents due to repeated starts and stops, leading to an abrupt decline in SoC during accelerating and recovery during braking. OCTBC presents a mix between substantial regenerative SoC recovery and urban energy demands.

The total EFCC per drive cycle is presented in Table 5. These tests involve repeated drive cycles until the cell voltage reaches lower cut-off voltage 2.5 V, which are idealized conditions for battery aging simulations. It is important to recognize that the values in this table represent the maximum degradation estimation for a cell subjected to extreme usage.

Table 5. EFCC per drive cycle.

Drive Cycle	Total EFCC per Drive Cycle
HHDDT	0.23
HWFET	0.15
US06	0.07
OCTBC	0.23

HHDDT and OCTBC drive cycles exhibit higher total EFCC value, which is consistent with their heavy-duty and urban transit profiles that typically involve higher energy demands. In contrast, HWFET, representing steady highway driving, its less demanding nature and more consistent energy usage. Despite its aggressive driving profile, US06 shows the lowest equivalence due to the corresponding current waveform presence of multiple short sub-segments within the cycle, where energy throughput is relatively low on average, thus reducing the overall total EFCC.

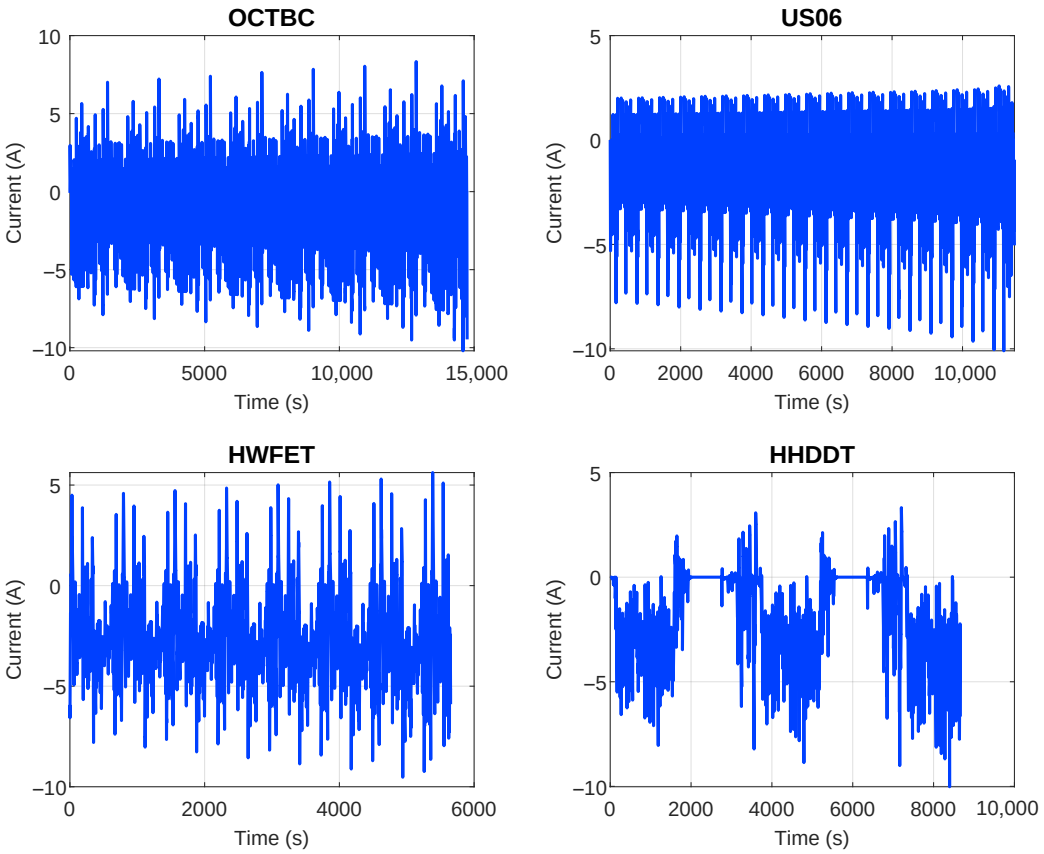


Figure 11. Current profiles of each drive cycle.

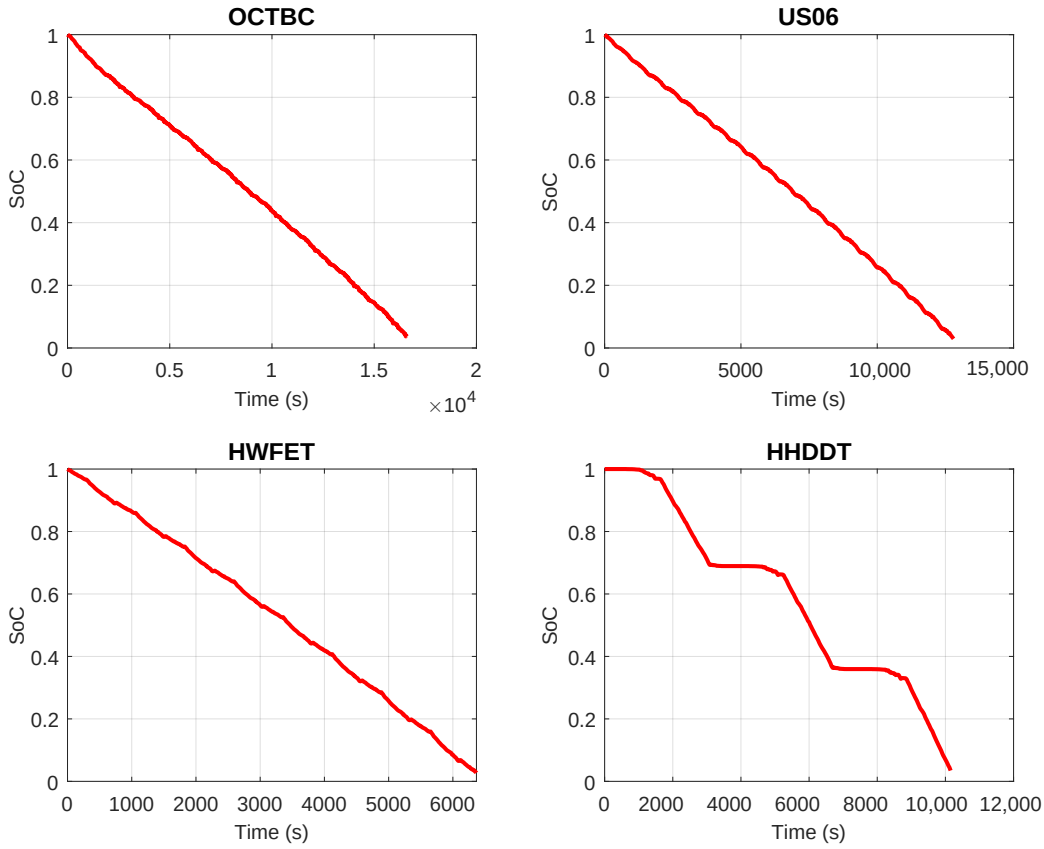


Figure 12. Variation of SoC for each drive cycle.

5. Evaluation Battery Degradation Using Simulated EIS Under Drive Cycles

This section investigates the impact on EIS results due to battery cycling subjected to the standard drive cycles. In the PyBaMM simulation a standard cycling protocol [9] is used for cycle ageing simulations. The standard cycling protocol involves three main steps: First, the battery is discharged at a rate of 1C until the voltage reaches 2.5 V. Next, the battery is charged at 0.3 C until the voltage reaches 4.2 V, Finally, the battery is held at 4.2 V until the current drops to C/100 at 298 K. This cycle is repeated to simulate battery aging over time. This standard cycling protocol is 0.89 of a total EFCC value. Table 6 outlines the number of standard drive cycles for each type of drive cycle for 100, 500 and 1000 simulated 'PyBaMM cycles'. Due to the low EFCC values per HWFET and US06 drive cycle, the standard drive cycle number to archive PyBaMM standard cycling protocol is high compared to HHDDT and OCTBC. The EIS results for the frequency band of 1 mHz to 1 kHz, highlight the influence of the different number of cycles in PyBaMM standard cycling protocol on battery degradation can be seen in Figure 13.

Table 6. Number Standard drive cycles for PyBaMM Simulated cycles.

Drive Cycle	No. of Standard Drive Cycle for 100 PyBaMM Simulated Cycles	No. of Standard Drive Cycle for 500 PyBaMM Simulated Cycles	No. of Standard Drive Cycle for 1000 PyBaMM Simulated Cycles
HHDDT	382	1910	3820
HWFET	577	2885	5770
US06	1243	6215	12,430
OCTBC	382	1910	3820

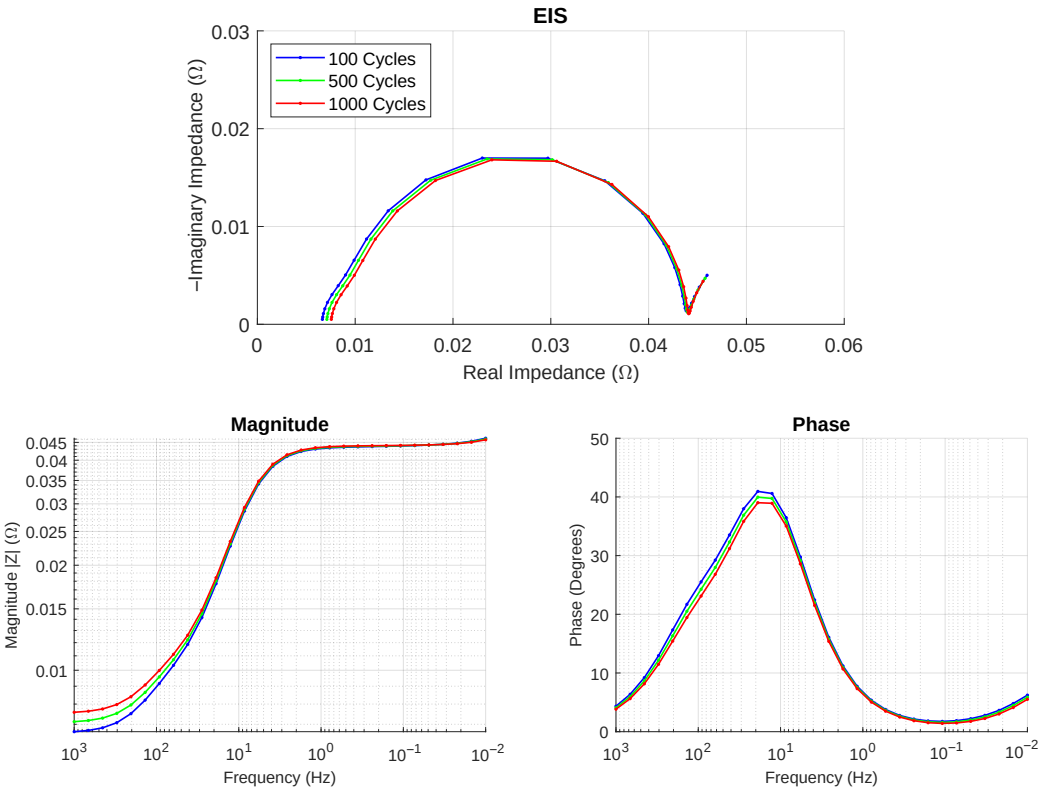


Figure 13. EIS for different PyBaMM simulated cycles at 298 K and 0.9 SoC.

For the further analysis of the impact of drive cycle characteristics on EIS results a fixed value of 150,000 km vehicle distance traveled (VDT) also referred to as the vehicle odometer reading, is considered for comparison. Using the standard metrics of the considered drive cycles and the equivalent cycle number calculation method discussed earlier, the total EFCC was obtained for the 150,000 km VDT and shown in Table 7.

Table 7. Total EFCC for 150,000 VDT.

Drive Cycle	Total EFCC for a VDT of 150,000 km
HTDDT	832
HWFET	1401
US06	832
OCTBC	3321

It can be seen that the HWFET has a higher total EFCC in lifetime compared to aggressive US06 and high load HHDDT due to the high distance per drive cycle. Due to repeated starts and stops the OCTBC drive cycle shows the highest total EFCC value.

As a result of the highest total EFCC value, the OCTBC drive cycle shows the greater impact on impedance changes as shown in Figure 14 due to abrupt decline in SoC during accelerating and recovery during braking. It has been noted that the total EFCC values of HWFET and US06 and HHDDT are closer compared to OCTBC. Accordingly the EIS variation between these drive cycles has only a slight difference.

The impedance variation also can be further analyzed based on frequency spectrum. Changes are minimal in the high-frequency range, indicating the stability of ohmic resistance, which mostly reflects the bulk characteristics of the battery materials. The mid-frequency region, however, experiences significant variations linked to changes in charge transfer resistance. This suggests that dynamic drive cycles, particularly those with aggressive acceleration and deceleration, magnify the stress on the electrochemical system. In the

low-frequency region, cycles with frequent current fluctuations, such as OCTBC, showed the greatest impedance growth, indicating severe impacts from SEI growth and lithium plating mechanisms.

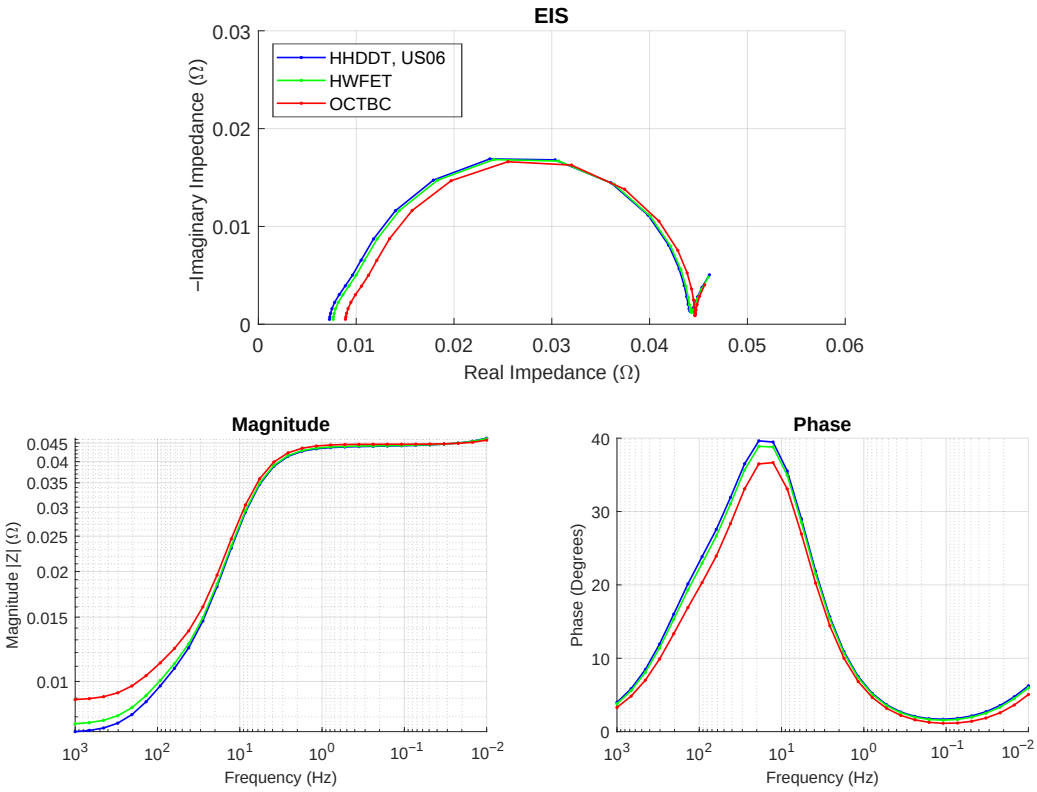


Figure 14. EIS for different drive cycles in minimum lifetime 298 K and 0.9 SoC.

6. Conclusions

This paper studies the simulated EIS characteristics of LIBs using SEI layer growth, lithium plating, and particle cracking models, coupled with a lumped thermal model and the DFN base model in PyBaMM [9]. Drive cycle analysis demonstrates that the repeated starts and stops in cycles such as OCTBC induced a greater impedance shift compared to other stable cycles like HWFET. The US06 with dynamic loading and HHDDT with high loading exhibited intermediate effects due to rapid SoC fluctuations. The results highlight the importance of coupling physics-based degradation models with drive cycle data to evaluate real-world operational conditions and their impact on battery health.

The integration of equivalent cycle counts derived from drive cycle data provided a robust method for assessing long-term performance and the change to EIS results due to degradation. Detailed electrochemical models, combined with degradation sub-models, are found to be an effective tool for analyzing battery ageing and estimating health under realistic operating conditions.

Furthermore, EIS-based SoH estimation presents a promising approach to tracking battery degradation. Key impedance parameters such as charge transfer resistance (R_{ct}) and SEI resistance (R_{SEI}) can be extracted by fitting the impedance spectrum to an equivalent circuit model. Specifically, R_{SEI} is obtained from the high-frequency semicircle in the Nyquist plot, representing SEI layer growth, while R_{ct} corresponds to the diameter of the intermediate-frequency semicircle, reflecting the resistance to charge transfer at the electrode-electrolyte interface. As the battery degrades, both resistances increase due to SEI thickening and slower electrode kinetics. By establishing a correlation between these impedance changes and capacity fade, a model for tracking SoH can be developed.

Future work will focus on refining these correlations and validating them under different cycling conditions.

Author Contributions: Conceptualization, A.E.J. and N.F.; methodology, A.E.J. and N.F.; software/simulation models, A.E.J.; investigation, A.E.J. and N.F. writing—original draft preparation, A.E.J. and N.F.; writing—review and editing, N.F., S.K., L.W. and J.P.K.; visualization, N.F., S.K., L.W. and J.P.K.; supervision, N.F., S.K., L.W. and J.P.K. All authors have read and agreed to the published version of the manuscript.

Funding: This research received no external funding.

Data Availability Statement: Data are contained within the article.

Conflicts of Interest: The authors declare no conflicts of interest.

Abbreviations

The following abbreviations are used in this manuscript:

LIB	Lithium-ion Battery
PyBaMM	Python Battery Mathematical Modeling
DFN	Doyle-Fuller-Newman Model
SEI	Solid Electrolyte Interface
SoC	State of Charge
EIS	Electrochemical Impedance Spectroscopy
RUL	Remaining Useful Life

References

1. Timilsina, L.; Badr, P.R.; Hoang, P.H.; Ozkan, G.; Papari, B.; Edrington, C.S. Battery Degradation in Electric and Hybrid Electric Vehicles: A Survey Study. *IEEE Access* **2023**, *11*, 42431–42462. [CrossRef]
2. Birkl, C.R.; Roberts, M.R.; McTurk, E.; Bruce, P.G.; Howey, D.A. Degradation diagnostics for lithium ion cells. *J. Power Sources* **2017**, *341*, 373–386. [CrossRef]
3. Diao, W.; Naqvi, I.H.; Pecht, M. Early detection of anomalous degradation behavior in lithium-ion batteries. *J. Energy Storage* **2020**, *32*, 101710. [CrossRef]
4. Zhang, Z.; Ji, C.; Liu, Y.; Wang, Y.; Wang, B.; Liu, D. Effect of Aging Path on Degradation Characteristics of Lithium-Ion Batteries in Low-Temperature Environments. *Batteries* **2024**, *10*, 107. [CrossRef]
5. Tomaszewska, A.; Chu, Z.; Feng, X.; O'Kane, S.; Liu, X.; Chen, J.; Ji, C.; Endler, E.; Li, R.; Liu, L.; et al. Lithium-ion battery fast charging: A review. *eTransportation* **2019**, *1*, 100011. [CrossRef]
6. Han, X.; Lu, L.; Zheng, Y.; Feng, X.; Li, Z.; Li, J.; Ouyang, M. A review on the key issues of the lithium ion battery degradation among the whole life cycle. *eTransportation* **2019**, *1*, 100005. [CrossRef]
7. Edge, J.S.; O'Kane, S.; Prosser, R.; Kirkaldy, N.D.; Patel, A.N.; Hales, A.; Ghosh, A.; Ai, W.; Chen, J.; Yang, J.; et al. Lithium ion battery degradation: What you need to know. *Phys. Chem. Chem. Phys.* **2021**, *23*, 8200–8221. [CrossRef] [PubMed]
8. Guo, J.; Li, Y.; Pedersen, K.; Stroe, D.I. Lithium-Ion Battery Operation, Degradation, and Aging Mechanism in Electric Vehicles: An Overview. *Energies* **2021**, *14*, 5220. [CrossRef]
9. O'Kane, S.E.J.; Ai, W.; Madabattula, G.; Alonso-Alvarez, D.; Timms, R.; Sulzer, V.; Edge, J.S.; Wu, B.; Offer, G.J.; Marinescu, M. Lithium-ion battery degradation: How to model it. *Phys. Chem. Chem. Phys.* **2022**, *24*, 7909–7922. [CrossRef] [PubMed]
10. Jayasinghe, A.E.; Fernando, N.; Kumarawadu, S.; Wang, L.; Karunadasa, J.P. Assessment of Lithium-Ion Battery Degradation and its impact on ECM using Simulated Impedance Spectroscopy. In Proceedings of the 2024 Energy Conversion Congress & Expo Europe (ECCE Europe), Darmstadt, Germany, 2–6 September 2024. [CrossRef]
11. Li, S.E.; Wang, B.; Peng, H.; Hu, X. An electrochemistry-based impedance model for lithium-ion batteries. *J. Power Sources* **2014**, *258*, 9–18. [CrossRef]
12. Iurilli, P.; Brivio, C.; Wood, V. On the use of electrochemical impedance spectroscopy to characterize and model the aging phenomena of lithium-ion batteries: A critical review. *J. Power Sources* **2021**, *505*. [CrossRef]
13. Motapon, S.N.; Lachance, E.; Dessaint, L.A.; Al-Haddad, K. A Generic Cycle Life Model for Lithium-Ion Batteries Based on Fatigue Theory and Equivalent Cycle Counting. *IEEE Open J. Ind. Electron. Soc.* **2020**, *1*, 207–217. [CrossRef]
14. Shui, Z.Y.; Li, X.H.; Feng, Y.; Wang, B.C.; Wang, Y. Combining Reduced-Order Model with Data-Driven Model for Parameter Estimation of Lithium-Ion Battery. *IEEE Trans. Ind. Electron.* **2023**, *70*, 1521–1531. [CrossRef]

15. Abu-Seif, M.A.; Abdel-Khalik, A.S.; Hamad, M.S.; Hamdan, E.; Elmalhy, N.A. Data-Driven modeling for Li-ion battery using dynamic mode decomposition. *Alex. Eng. J.* **2022**, *61*, 11277–11290. [CrossRef]
16. Diao, W.; Saxena, S.; Pecht, M. Accelerated cycle life testing and capacity degradation modeling of $LiCoO_2$-graphite cells. *J. Power Sources* **2019**, *435*, 226830. [CrossRef]
17. Diao, W.; Kim, J.; Azarian, M.H.; Pecht, M. Degradation modes and mechanisms analysis of lithium-ion batteries with knee points. *Electrochim. Acta* **2022**, *431*, 141143. [CrossRef]
18. Zhu, C.; Sun, L.; Chen, C.; Tian, J.; Shen, W.; Xiong, R. Lithium-ion battery degradation diagnosis and state-of-health estimation with half cell electrode potential. *Electrochim. Acta* **2023**, *459*, 142588. [CrossRef]
19. Sulzer, V.; Marquis, S.G.; Timms, R.; Robinson, M.; Chapman, S.J. Python Battery Mathematical Modelling (PyBaMM). *J. Open Res. Softw.* **2021**, *9*, 14. [CrossRef]
20. Kirk, T.L.; Lewis-Douglas, A.; Howey, D.; Please, C.P.; Jon Chapman, S. Nonlinear Electrochemical Impedance Spectroscopy for Lithium-Ion Battery Model Parameterization. *J. Electrochem. Soc.* **2023**, *170*, 010514. [CrossRef]
21. Meddings, N.; Heinrich, M.; Overney, F.; Lee, J.S.; Ruiz, V.; Napolitano, E.; Seitz, S.; Hinds, G.; Raccichini, R.; Gaberšček, M.; et al. Application of electrochemical impedance spectroscopy to commercial Li-ion cells: A review. *J. Power Sources* **2020**, *480*, 228742. [CrossRef]
22. Liu, L.; Zhu, M. Modeling of SEI Layer Growth and Electrochemical Impedance Spectroscopy Response using a Thermal-Electrochemical Model of Li- ion Batteries. *ECS Trans.* **2014**, *61*, 43. [CrossRef]
23. Eddahech, A.; Briat, O.; Bertrand, N.; Delétage, J.Y.; Vinassa, J.M. Behavior and state-of-health monitoring of Li-ion batteries using impedance spectroscopy and recurrent neural networks. *Int. J. Electr. Power Energy Syst.* **2012**, *42*, 487–494. [CrossRef]
24. Xiong, R.; Tian, J.; Mu, H.; Wang, C. A systematic model-based degradation behavior recognition and health monitoring method for lithium-ion batteries. *Appl. Energy* **2017**, *207*, 372–383. [CrossRef]
25. Stroe, D.I.; Swierczynski, M.; Stan, A.I.; Knap, V.; Teodorescu, R.; Andreasen, S.J. Diagnosis of lithium-ion batteries state-of-health based on electrochemical impedance spectroscopy technique. In Proceedings of the 2014 IEEE Energy Conversion Congress and Exposition (ECCE), Pittsburgh, PA, USA, 14–18 September 2014. [CrossRef]
26. Galeotti, M.; Cinà, L.; Giammanco, C.; Cordiner, S.; Di Carlo, A. Performance analysis and SOH (state of health) evaluation of lithium polymer batteries through electrochemical impedance spectroscopy. *Energy* **2015**, *89*, 678–686. [CrossRef]
27. Liu, Y.; Liu, C.; Liu, Y.; Sun, F.; Qiao, J.; Xu, T. Review on degradation mechanism and health state estimation methods of lithium-ion batteries. *J. Traffic Transp. Eng. (Engl. Ed.)* **2023**, *10*, 578–610. [CrossRef]
28. Zhang, Q.; Huang, C.G.; Li, H.; Feng, G.; Peng, W. Electrochemical Impedance Spectroscopy Based State-of-Health Estimation for Lithium-Ion Battery Considering Temperature and State-of-Charge Effect. *IEEE Trans. Transp. Electrif.* **2022**, *8*, 4633–4645. [CrossRef]
29. Eddahech, A.; Briat, O.; Woirgard, E.; Vinassa, J.M. Remaining useful life prediction of lithium batteries in calendar ageing for automotive applications. *Microelectron. Reliab.* **2012**, *52*, 2438–2442. [CrossRef]
30. Wang, X.; Wei, X.; Dai, H. Estimation of state of health of lithium-ion batteries based on charge transfer resistance considering different temperature and state of charge. *J. Energy Storage* **2019**, *21*, 618–631. [CrossRef]
31. Zhao, L.; Wang, Y.; Cheng, J. A Hybrid Method for Remaining Useful Life Estimation of Lithium-Ion Battery with Regeneration Phenomena. *Appl. Sci.* **2019**, *9*, 1890. [CrossRef]
32. Jayasinghe, A.E.; Fernando, N.; Kumarawadu, S.; Wang, L. Review on Li-ion Battery Parameter Extraction Methods. *IEEE Access* **2023**, *11*, 73180–73197. [CrossRef]
33. Single, F.; Latz, A.; Horstmann, B. Identifying the Mechanism of Continued Growth of the Solid-Electrolyte Interphase. *ChemSusChem* **2018**, *11*, 1950–1955. [CrossRef] [PubMed]
34. Yang, X.G.; Leng, Y.; Zhang, G.; Ge, S.; Wang, C.Y. Modeling of lithium plating induced aging of lithium-ion batteries: Transition from linear to nonlinear aging. *J. Power Sources* **2017**, *360*, 28–40. [CrossRef]
35. Yang, X.G.; Ge, S.; Liu, T.; Leng, Y.; Wang, C.Y. A look into the voltage plateau signal for detection and quantification of lithium plating in lithium-ion cells. *J. Power Sources* **2018**, *395*, 251–261. [CrossRef]
36. Deshpande, R.; Verbrugge, M.; Cheng, Y.T.; Wang, J.; Liu, P. Battery Cycle Life Prediction with Coupled Chemical Degradation and Fatigue Mechanics. *J. Electrochem. Soc.* **2012**, *159*, A1730–A1738. [CrossRef]
37. Marquis, S.G.; Sulzer, V.; Timms, R.; Please, C.P.; Chapman, S.J. An Asymptotic Derivation of a Single Particle Model with Electrolyte. *J. Electrochem. Soc.* **2019**, *166*, A3693. [CrossRef]
38. Li, R.; Kirkaldy, N.; Oehler, F.; Marinescu, M.; Offer, G.J.; O'Kane, S.E.J. Lithium-ion battery degradation: Validating lifetime prediction modelling. *arXiv* **2023**, arXiv:2311.05482.
39. Li, R.; O'Kane, S.; Marinescu, M.; Offer, G.J. Modelling Solvent Consumption from SEI Layer Growth in Lithium-Ion Batteries. *J. Electrochem. Soc.* **2022**, *169*, 060516. [CrossRef]
40. Li, R.; O'Kane, S.; Huang, J.; Marinescu, M.; Offer, G.J. A million cycles in a day: Enabling high-throughput computing of lithium-ion battery degradation with physics-based models. *J. Power Sources* **2024**, *598*, 234184. [CrossRef]

41. Chen, C.H.; Brosa Planella, F.; O'Regan, K.; Gastol, D.; Widanage, W.D.; Kendrick, E. Development of Experimental Techniques for Parameterization of Multi-scale Lithium-ion Battery Models. *J. Electrochem. Soc.* **2020**, *167*, 080534. [CrossRef]
42. Parschau, A.; Degler, D.; Fill, A.; Birke, K.P.; Allmendinger, F. Cycle Tests on the Influence of Different Charging Currents—A Case Study on Different Commercial, Cylindrical Lithium Ion Cells. *Batteries* **2023**, *9*, 83. [CrossRef]
43. O'Kane, S.E.J.; Campbell, I.D.; Marzook, M.W.J.; Offer, G.J.; Marinescu, M. Physical Origin of the Differential Voltage Minimum Associated with Lithium Plating in Li-Ion Batteries. *J. Electrochem. Soc.* **2020**, *167*, 090540. [CrossRef]
44. Hallemans, N.; Courtier, N.E.; Please, C.P.; Planden, B.; Dhoot, R.; Timms, R.; Howey, D.; Duncan, S.R. Physics-based battery model parametrisation from impedance data. *arXiv* **2024**, arXiv:2412.10896.
45. Wimarshana, B.; Bin-Mat-Arishad, I.; Fly, A. A multi-step parameter identification of a physico-chemical lithium-ion battery model with electrochemical impedance data. *J. Power Sources* **2023**, *580*, 233400. [CrossRef]
46. Andre, D.; Meiler, M.; Steiner, K.; Walz, H.; Soczka-Guth, T.; Sauer, D.U. Characterization of high-power lithium-ion batteries by electrochemical impedance spectroscopy. II: Modelling. *J. Power Sources* **2011**, *196*, 5349–5356. [CrossRef]
47. Yao, J. *Lithium-Ion Battery Drive Cycle Dataset*; Technische Universität Berlin: Berlin, Germany, 2024. [CrossRef]
48. National Renewable Energy Laboratory (NREL). *DriveCAT: Drive Cycle Analysis Tool*; NREL: Applewood, CO, USA, 2024.

Disclaimer/Publisher's Note: The statements, opinions and data contained in all publications are solely those of the individual author(s) and contributor(s) and not of MDPI and/or the editor(s). MDPI and/or the editor(s) disclaim responsibility for any injury to people or property resulting from any ideas, methods, instructions or products referred to in the content.